ISSN 2095-9281 (网络)
ISSN 2095-9273 (印刷)
科学通报 (英文版)

Science Bulletin

Volume 70 · Number 24 · December **2025**

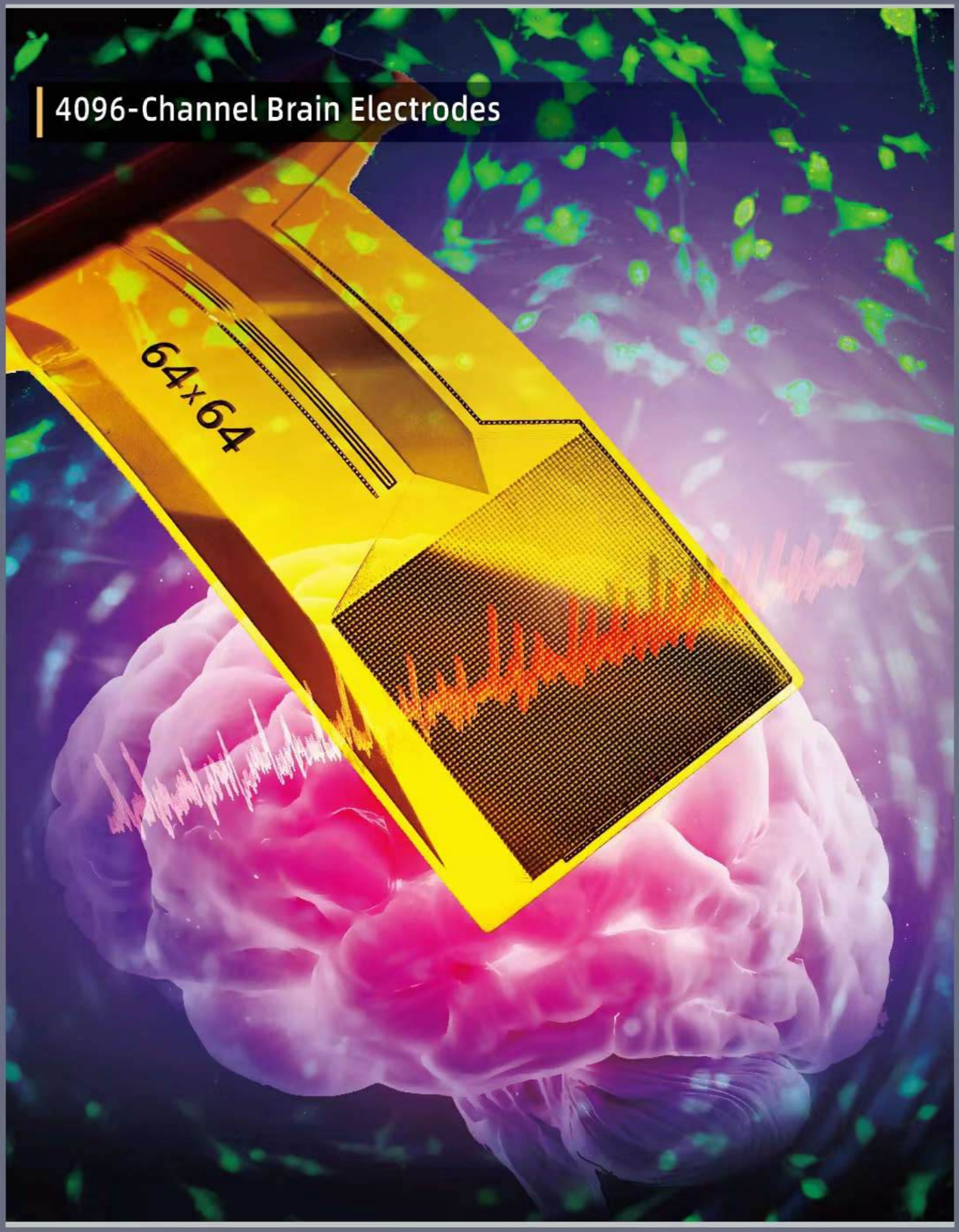

www.scibull.com

Science Bulletin 70 (2025) 4133–4137

Contents lists available at ScienceDirect

Science Bulletin

journal homepage: www.elsevier.com/locate/scib

Short Communication

High-resolution spatial mapping of electrocorticographic activities with NeuroCam: a 4096-channel, multiplexed flexible thin-film transistor array

Yang Xie [a,b], Zepeng Zhang [c], Muyang Liu [a], Jinhong Guo [a], Miao Xu [d,e], Lei Zhou [d,e], Lei Zhang [f,g], Lihao Yao [a], Xiaolin Zhou [h], Zhengwei Hu [h], Liang Ma [i], Xiaojian Li [h], Yongxiang Guo [j], Jiaxin Lei [j], Yue Cao [j], Milin Zhang [k], Huachun Wang [l], He Ding [m], Xin Fu [n], Quanlei Liu [o], Yihe Wang [o], Lan Yin [n], Guoguang Zhao [o,*], Xing Sheng [a,*]

[a] *Department of Electronic Engineering, Beijing National Research Center for Information Science and Technology, Institute for Precision Medicine, Laboratory of Flexible Electronics Technology, IDG/McGovern Institute for Brain Research, Tsinghua University, Beijing 100084, China*
[b] *Nanjing Research Institute of Electronics Technology, Nanjing 210039, China*
[c] *NeuCyber NeuroTech (Beijing) Co., Ltd., Beijing 102206, China*
[d] *The Institute of Polymer Optoelectronic Materials and Devices, South China University of Technology, Guangzhou 510640, China*
[e] *Guangzhou New Vision Optoelectronic Company Ltd., Guangzhou 510530, China*
[f] *School of Biomedical Engineering, Capital Medical University, Beijing 100069, China*
[g] *Chinese Institute for Brain Research, Beijing (CIBR), Beijing 102206, China*
[h] *Shenzhen-Hong Kong Institute of Brain Science-Shenzhen Fundamental Research Institutions, Shenzhen Institute of Advanced Technology, Chinese Academy of Sciences, Shenzhen 518055, China*
[i] *Shenzhen We-Linking Medical Technology Co., Ltd., Shenzhen 518000, China*
[j] *Department of Electronic Engineering, Tsinghua University, Beijing 100084, China*
[k] *Department of Electronic Engineering, Institute for Precision Medicine, Tsinghua University, Beijing 100084, China*
[l] *School of Integrated Circuits, Shenzhen Campus of Sun Yat-sen University, Shenzhen 518107, China*
[m] *Beijing Engineering Research Center of Mixed Reality and Advanced Display, School of Optics and Photonics, Beijing Institute of Technology, Beijing 100081, China*
[n] *School of Materials Science and Engineering, The Key Laboratory of Advanced Materials of Ministry of Education, State Key Laboratory of New Ceramics and Fine Processing, Laboratory of Flexible Electronics Technology, Tsinghua University, Beijing 100084, China*
[o] *Department of Neurosurgery, Xuanwu Hospital, Capital Medical University, Beijing 100053, China*

ARTICLE INFO

Article history:
Received 18 June 2025
Received in revised form 5 October 2025
Accepted 10 November 2025
Available online 17 November 2025

Realizing precise recording with large populations of neurons has been a long-standing goal in developing next-generation brain-machine interfaces (BMIs) [1,2]. Specifically, flexible electrocorticography (ECoG) devices placed on the cerebral cortex provide a nonpenetrating means to measure population-level coordinated neural activities across wide cortical areas, and have been successfully applied for speech synthesis, motor decoding, and seizure localization [3]. While conventional ECoG electrodes are typically a few millimeters in size, cortical columns sharing certain functional and anatomical properties have lateral dimensions ranging from tens to hundreds of micrometers [4]. Moreover, experimental evidences prove that high-resolution ECoG recordings markedly improve the accuracy of neural decoding [5]. Therefore, tremendous efforts focus on the innovation of thin-film, high-density microscale ECoG (μECoG) electrode arrays with over hundreds and even thousands of readout channels to obtain high-throughput brain activity mapping at a submillimeter resolution [2]. However, in passive neural electrodes, each recording channel requires at least one independent wire for signal readout, imposing formidable challenges for device fan-in/fan-out and scaling up high-density arrays.

By contrast, active neural electrode arrays resolve the above-mentioned issue by time-division multiplexing, offering a viable solution to achieving high-density, high-throughput μECoG devices. Representative works include the development of flexible μECoG recording arrays integrated with thin-film transistor (TFT) based multiplexers made of monocrystalline silicon (Si) [6,7], graphene [8] and organic semiconductors [9]. Nevertheless, the production of these devices involves sophisticated or non-standard manufacturing processes, impeding their cost-effective fabrication

* Corresponding authors.
E-mail addresses: ggzhao@ccmu.edu.cn (G. Zhao), xingsheng@tsinghua.edu.cn (X. Sheng).

https://doi.org/10.1016/j.scib.2025.11.030

with uniform performance on a large scale. Alternatively, metal oxide semiconductor based TFTs, which have been widely used in display technologies, are fully compatible with low-cost, meter-scale production on flexible platforms and provide a promising solution to large-area, multiplexed biological sensing. Prominent examples involve recently reported indium gallium zinc oxide (IGZO) TFT arrays for *in vitro* cultured cell sensing [10] or *in vivo* μECoG recording [11]; however, flexible high-throughput (> 1000 channels) μECoG devices made of oxide-based TFTs have not yet been realized for *in vivo* brain recording.

In this study, we report a flexible, multiplexed high-density μECoG array named NeuroCam for high-throughput brain activity mapping. NeuroCam features 4096 recording channels and an electrode density of 44 sites/mm^2 based on a metal-oxide TFT array. The actively multiplexed scheme operates with only 128 input/output wires, effectively addressing the interconnection difficulties. *In vitro* and *in vivo* experiments demonstrate ideal biocompatibilities of the flexible device system. Validated in a rabbit model of epilepsy, NeuroCam records spatially resolved neural activities across extensive cortical areas. The high-density array precisely maps the temporal evolution of epileptiform spikes as well as the spatial distribution of the epileptogenic zone. This device concept provides a promising route towards high-density, high-throughput BMI systems compatible with industrial-scale production and brings unprecedented opportunities for both neuroscience and neuroengineering.

NeuroCam is based on a lanthanide-doped InZnO (Ln-IZO) TFT array comprising 4096-pixel units arranged in a 64-row by 64-column grid, specifically designed for high spatial resolution ECoG acquisition. The fully fabricated flexible NeuroCam array has a total thickness of less than 30 μm and an active area of 9.6 mm × 9.6 mm (Fig. 1a). Each pixel measures 150 μm × 150 μm, and the size of the Au sensing pad is 70 μm × 135 μm (Fig. 1b). The manufacturing process is performed in an industrial-scale production line, which ensures desirable device scalability and uniformity over a large substrate (20 cm × 20 cm) with a high yield (Fig. S1 online). From bottom to top, the device structure (Fig. 1c) comprises a flexible polyimide (PI) substrate (25 μm thick), an active layer of Ln-IZO TFT array, multilayered organic/inorganic encapsulants and molybdenum (Mo) based interconnect electrodes, and gold (Au) based sensing pads. Fig. 1c shows schematic as well as cross-sectional scanning electron microscopic (SEM) images illustrating detailed device layouts. Overall, the NeuroCam array presents the highest channel count (4096) and density (44 sites/mm^2) compared with state-of-the-art multiplexed μECoG techniques that have been validated in *in vivo* experiments (Fig. 1d and Table S1 online). Based on electrical characterizations in Fig. 1e, we determine that the Ln-IZO TFT has a mobility of 15.13 cm^2/(V s) and a threshold voltage of 2.7 V. When turn-on voltage and turn-off gate voltages (V_{gs}) are set at 6 and −2 V, respectively, the TFT achieves an on/off ratio of about 6×10^6. Fig. 1f plots the frequency response of V_{out}/V_{in} for a typical TFT in the array, which is collected by changing the input signal (V_{in}) frequency from 10 Hz to 40 kHz and measuring the collected output voltage (V_{out}) via the S port. The obtained 3 dB attenuation frequency exceeds 1 kHz, which is much higher than the typical frequency range of ECoG signals (< 200 Hz). The device's frequency dependent impedance is further measured in the PBS solution, and its value is around 100 kΩ at 1–100 kHz (Fig. S2 online).

The working principles of the multiplexed array are illustrated in Fig. 1g–i. In a single TFT, the drain (D) with the sensing electrode contacts brain tissue, the source (S) connects to the external output, and conduction is controlled by toggling the gate (G) between on and off states (Fig. 1g). In the full array, 64 source lines are shared by 64 channels each, selected by scanning the corresponding gate lines, enabling 4096-channel operation with only 128 I/O lines (Fig. 1h). During acquisition, G lines are activated sequentially to enable time-division multiplexed recording across all channels (Fig. 1i).

We further evaluate the device's noise levels in both static and dynamic modes. In the static mode, one G line remains open while others are closed, and noise levels are determined at different sampling rates and precision modes (Fig. S3 online). When operated in the high-precision mode, the recording system is capable to collect data from a maximum of 24 S lines. In this case, the system reaches the lowest root mean square (RMS) noise level of 2.3 ± 0.3 μV at a sampling rate of 100 kS/s (Fig. S3b online). Similar to previous works [12], this static mode is specifically designed for high-precision recordings from small regions within the array's coverage and demonstrates the lowest achievable noise level under controlled conditions. Dynamic scanning performed in the full 64 × 64 array leads to elevated noise levels (Fig. S4 online) comparable to previously reported μECoG arrays with similar multiplexing systems [6,7]. Besides supporting an unprecedented channel count of 4096—significantly exceeding that of any previously reported system—our platform maintains an acceptable RMS noise level during dynamic scanning (63.6 ± 24.1 μV_{rms}). At reduced channel counts, the noise decreases substantially (8.8 ± 4.2 μV_{rms} at 384 channels and 12.6 ± 8.4 μV_{rms} at 1536 channels), comparable or superior to previously reported systems (e.g., 2.65 μV_{rms} at 256 channels [11], 58 μV_{rms} at 1008 channels [7]). The slightly higher noise in the full 4096-channel configuration reflects the expected trade-off for achieving such unprecedented scalability.

In such a multiplexed array, each 64 input and 64 output channels share the same gate line and the same source line, respectively. Therefore, crosstalk signals may exist among pixels. In Fig. S5 and Movie S1 (online), we evaluate the system's crosstalk by applying an input signal on a single pixel and mapping the entire array. Adjacent pixels in the direction of the source line receive higher crosstalks (−12.6 dB) comparing to those in the direction of gate line (−37.2 dB), while second nearest neighboring and further pixels show minimal crosstalks (−45 dB), suggesting induced artifacts are below the noise floor for weak events and removable by standard processing.

The histogram of NeuroCam illustrates uniformly distributed performance among 4096 channels, with a gain (V_{out}/V_{in}) of 0.78 ± 0.12 (Fig. 2a). Additionally, we emulate spatially resolved bioelectric signals by applying a sinusoidal wave (1 mVpp, 18 Hz) via a PBS droplet on the array (Fig. 2b). The mapping results clearly demonstrate the NeuroCam's capability of dynamically recording electric signals with desirable spatial and temporal resolutions in the aqueous environment (Fig. 2c, Fig. S6 and Movie S2 online).

Furthermore, we conduct systematic characterizations to evaluate the NeuroCam's biocompatiblites. First, cytotoxicity tests show no significant difference in cell viability between the TFT array and glass (Fig. S7 online). Second, the infrared thermal imaging reveals negligible temperature rises upon the device operation, suggesting that the device array would not impose any adverse thermal effects on the brain tissue (Fig. S8 online). Third, the flexible NeuroCam array maintains stable performance under deformation, with device yield and gain changed slightly after 10,000 bending cycles (Fig. S9 online). Last, the array presents modest chronic reliability, with the device yield changing from 100% to ~80% and a stable gain among all the channels after soaking in PBS solution at 37 °C for two weeks. Furthermore, survived devices exhibited stable electrical performance, as evidenced by consistent signal amplitude, noise level, and signal-to-noise ratio across all channels throughout the immersion period (Fig. S10 online).

Epilepsy is a common neurological disorder marked by abnormal neuronal discharges in the brain. Monitoring these neural activities across wide brain regions with high spatial resolution is

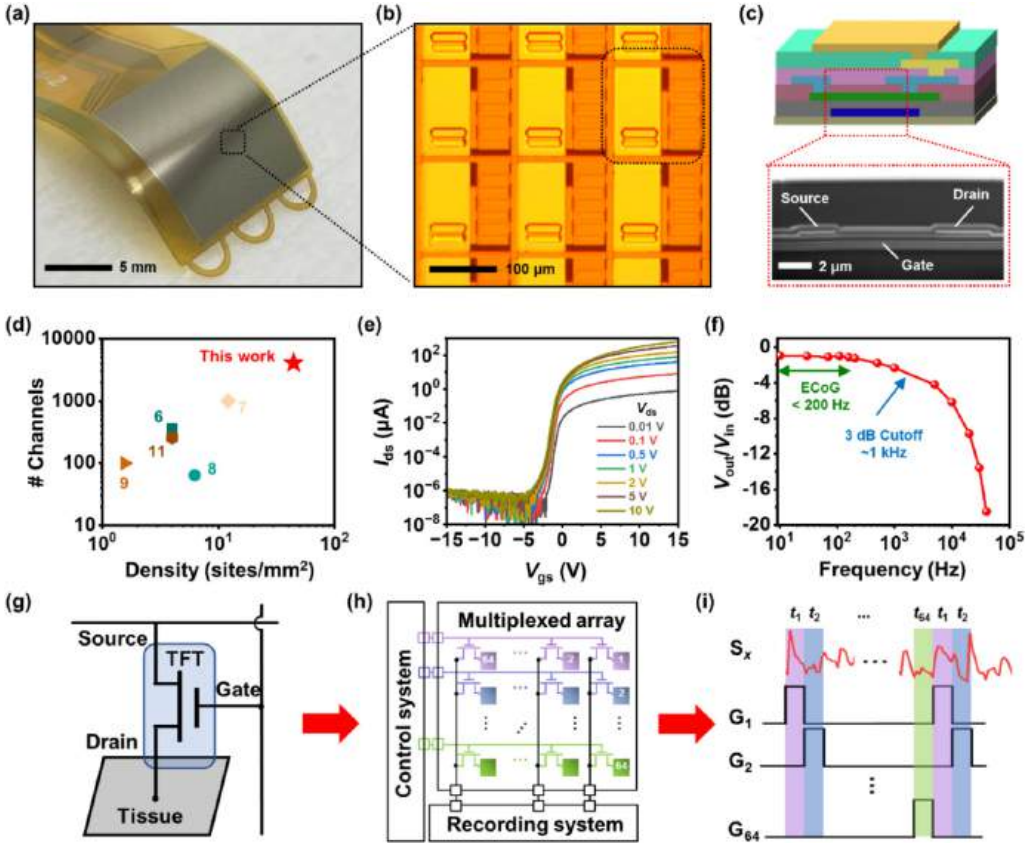

Fig. 1. The NeuroCam: a flexible, 4096-channel multiplexed μECoG device array. (a, b) Optical and zoomed-in microscopic photographs of a NeuroCam array. The dimensions of each pixel unit and corresponding Au sensing pad are 150 μm × 150 μm and 135 μm × 70 μm, respectively. (c) Schematic diagram and corresponding cross-sectional SEM image showing the detailed structure of a single recording unit. The topmost Au pad serves as the sensing electrode, connected to the TFT drain electrode through a stepwise via structure made of multilayered Mo based interconnects and organic/inorganic encapsulation layers. The bottom substrate is made of PI (25 μm thick). (d) Comparison of the NeuroCam array with existing multiplexed μECoG arrays used for *in vivo* experiments, in terms of their channel number and density. (e) Transfer characteristic curve of a representative TFT under different V_{ds}. (f) Measured frequency characteristics of a recording channel, showing a 3 dB cutoff at ~1 kHz. Here the G line is kept on, while a 10 mVpp sinusoidal wave signal of varying frequencies is applied to the drain exposed in PBS. (g–i) Operational principle of the NeuroCam array. (g) Single unit: The drain electrode of the TFT device directly contacts with brain tissue, the gate controls the conduction between the drain and the source, and the source connects to the external recording system. (h) TFT array: The recording system continuously collects data from all the source (S) lines, while the control system modulates all the gate (G) lines, by sequentially turning on one G line (V_{on} = +6 V) and keeping other G lines at the off state (V_{off} = −2 V). (i) Collected results: The time-domain control signals (G_1 to G_{64}) segment the collected data, enabling time-division multiplexed recording in a specific S line (S_x) cyclically repeating from t_1 to t_{64} (t = 62.5 μs for each channel).

crucial for understanding mechanisms of epileptogenesis, identifying the epileptogenic zone, and improving treatment strategies [6,13]. Here we utilize the NeuroCam array to record ECoG signals in a rabbit model with epilepsy (Fig. 2d). In anesthetized animals, intracortical administration of penicillin induces focal epilepsy, and the subdurally positioned 4096-channel NeuroCam array covers a wide cortical area including the injection site (Fig. 2e and Fig. S11 online). Fig. S12 (online) shows ECoG signals and time–frequency patterns from a representative channel near the injection site at different time points.

The full mapping results from all the 4096 channels in the array, as shown in Fig. 2f, clearly illustrate the spatial differentiation of ECoG activities. Electrodes near the injection site exhibit similar activity, indicating the propagation of synchronized epileptic discharges, which may also be influenced by crosstalk from the multiplexed scanning system. Among the various electrophysiological characteristics of epileptic seizures, focal intense abnormal activity is the most specific biomarker. The regions with the most intense spike signals closely correlate with the location of the injection point. In these active regions, bilateral spikes occur with a burst frequency of ~3 Hz, a duration of ~150 ms, and a peak-to-peak amplitude of ~2 mV. By contrast, ECoG signals collected by channels distant from the injection point (specifically, in the contralateral hemisphere) exhibit much weaker activities.

The NeuroCam array provides a large coverage and high spatial resolution ECoG mapping, enabling the capture of intricate local and global dynamics during epileptic seizures on the cortical surface. This reflects the characteristic large-scale synchronized discharges during epileptic activity. The high-density mapping across extensive brain regions reveals detailed spatial and temporal evolution of seizure activities (Fig. 2g, Figs. S13, S14, Movie S3 online). In epileptic seizures, ECoG signal propagation is accompanied by large-scale synchronized discharges, with regions often spanning millimeter scales [14]. Despite the array's 150-μm pitch, the larger spatial scale of the epileptic focus likely results in observed activity islands near 1 mm. However, detailed analysis of the mapping images reveals clear submillimeter differences between channels. These time-lapse mapping results clearly illustrate the developmental process of abnormal electrical discharges during an epileptic event across the brain: (i) the seizure spike initially arises near the focal area; (ii) the focal area shows a positive potential that propagates abnormal signals outward, with the positive signal spreading to the lower-left ipsilateral brain region and the negative potential extending to the contralateral hemisphere; (iii) abnormal electrical waves spread throughout the entire area covered by the array, with the focal area shifting to a negative signal and gradually spreading the same waveform to adjacent ipsilateral regions; (iv) the electrical activity subsides, with only

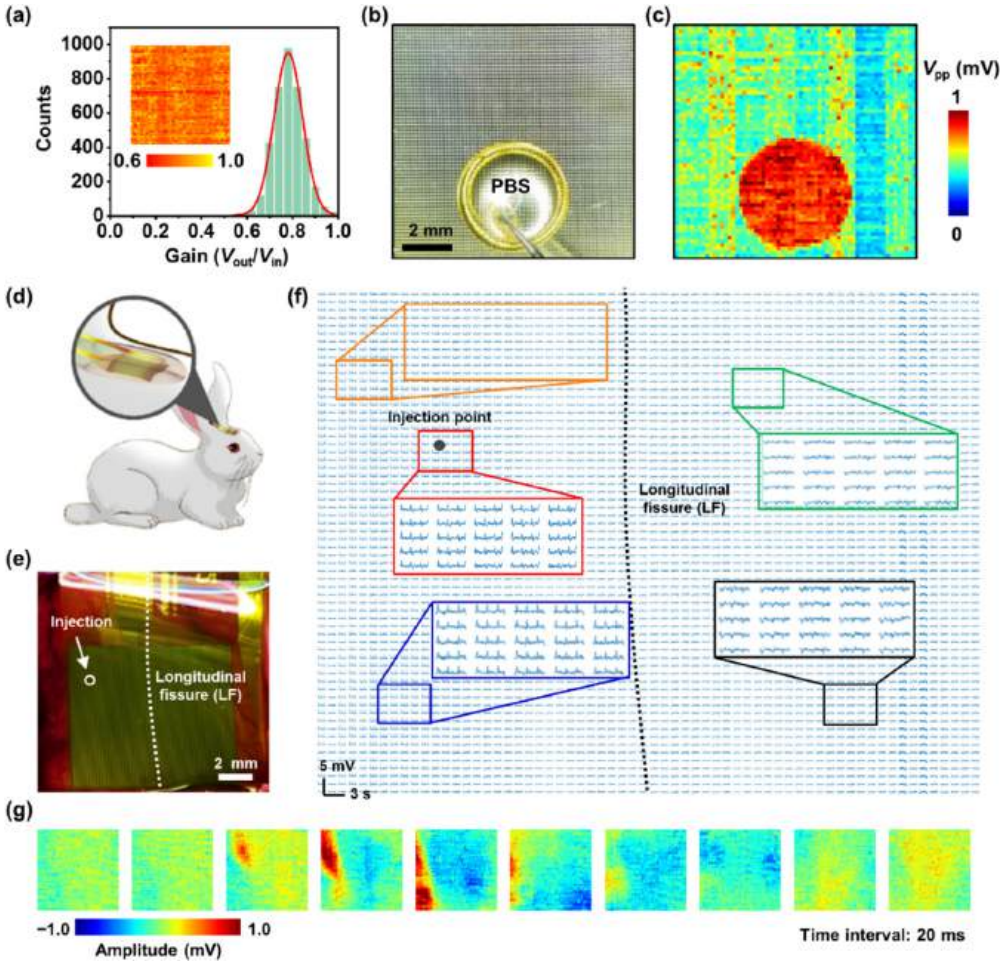

Fig. 2. High-spatial-resolution ECoG mapping using the NeuroCam array. (a) Gain (V_{out}/V_{in}) characteristics of all the 4096 channels in the array in PBS. The input signal is a sine wave with an amplitude of 1 mV and a frequency of 12 Hz. (b) Photograph of a NeuroCam array with a droplet of PBS on its surface. (c) Mapping results of spatially resolved output signals when injecting a 1 mVpp sine signal (18 Hz) into PBS. (d) Schematic diagram and (e) top-view photograph illustrating a NeuroCam array mounted on the cortex of a rabbit. The arrow indicates the location of penicillin injection. (f) ECoG activities recorded from all 4096 channels in the array, during status epilepticus in the rabbit. Insets show enlarged plots from different brain regions. (g) Time-lapse ECoG mapping of an individual spike, with a total duration of 180 ms.

mild oscillations in certain regions of both hemispheres. This pattern of large spikes followed by slower waves of opposite polarity aligns with previously reported results of focal epilepsy [15]. Band-pass filtering of the epileptic waveforms into different frequency ranges reveals distinct time–frequency oscillations associated with spike bursts (Fig. S15 online). Furthermore, the high-density NeuroCam array allows sub-millimeter spatial correlation analysis of ECoG signals, demonstrating distance-dependent correlation decay and pronounced S-line crosstalk under multiplexed operation (Fig. S16 online).

In conclusion, we developed the 4096-channel NeuroCam system based on flexible, active TFT arrays, and demonstrated its capability for high-throughput ECoG recording across large brain areas in epileptic rabbits. Compared to previously reported multiplexed μECoG arrays demonstrated for *in vivo* studies, our NeuroCam system presents superior features in terms of its channel number (4096) and density (44 sites/mm^2). Its high spatial resolution and extensive coverage provide practical advantages for precisely analyzing the spatiotemporal progression of epileptiform abnormalities and localizing epileptogenic zones. Additionally, understanding the differential and correlational patterns across brain regions during specific physiological activities can offer crucial insights into unraveling complex neural circuitry. On the other hand, the high-density, submillimeter electrodes would be particularly valuable in exploring correlations between cortical columns (in size from tens to hundreds of micrometers) and decoding complex behaviors like movement, sensing, and vision [4]. Moreover, since the multiplexing strategy has effectively resolved the wiring issue of passive μECoG electrodes, the mature manufacturing process of flexible TFTs could readily boost the channel number from the kilo scale (10^3) to the mega scale (10^6) in the near future. For neurophysiological applications, long-term *in vivo* studies are necessary to validate the device's stability and biocompatibility. In addition, the device geometry and flexibility can be further optimized for studying complex cortical topographies (sulci and gyri) in primates. To summarize, the presented device design and production strategies pave the way for next-generation, high-performance BMI technologies and will bring unprecedented opportunities to neuroscience and neuroengineering.

Conflict of interest

The authors declare that they have no conflict of interest.

Acknowledgments

This work was supported by the Beijing Municipal Natural Science Foundation (L246017 and Z220015), the National Natural

Science Foundation of China (NSFC) (T2425003, 52272277, 92164202, 62304264, T2122010, and 52171239), NeuCyber NeuroTech (Beijing) Company, China (NC-2023-HE-02), Tsinghua University Initiative Scientific Research Program (2024Z02ORD001), the Science and Technology Program of Guangzhou City (2024B01J0079), and the Beijing Nova Program (20230484254). The device fabrication and characterization work is supported by the Center of Intelligent Sensing and Precise Testing Technology in Optics and Photonics, Beijing Institute of Technology, and Tsinghua Nanofabrication Technology Center.

Author contributions

Yang Xie, Jinhong Guo, Muyang Liu, Miao Xu, Lei Zhou, and Xing Sheng performed device design, fabrication, and characterization. Yang Xie, Muyang Liu, Jinhong Guo, Lihao Yao, Xiaolin Zhou, Yongxiang Guo, Jiaxin Lei, Yue Cao, Xiaojian Li, Milin Zhang, and Xing Sheng designed and tested circuits. Yang Xie, Zepeng Zhang, Muyang Liu, Jinhong Guo, Zhengwei Hu, Xin Fu, Quanlei Liu, Yihe Wang, and Xing Sheng designed and performed biological experiments. Yang Xie, Muyang Liu, Jinhong Guo, Liang Ma, and Xing Sheng performed data processing. Lei Zhang, Xiaojian Li, Milin Zhang, Huachun Wang, He Ding, Lan Yin, Guoguang Zhao, and Xing Sheng provided tools and supervised the research. Yang Xie and Xing Sheng wrote the paper in consultation with other authors.

Appendix A. Supplementary material

Supplementary data to this article can be found online at https://doi.org/10.1016/j.scib.2025.11.030.

References

[1] Chang EF. Towards large-scale, human-based, mesoscopic neurotechnologies. Neuron 2015;86:68–78.
[2] Xie Y, Peng Y, Guo J, et al. Materials and devices for high-density, high-throughput micro-electrocorticography arrays. Fundam Res 2025;5:17–28.
[3] Zhao ET, Hull JM, Mintz Hemed N, et al. A CMOS-based highly scalable flexible neural electrode interface. Sci Adv 2023;9:eadf9524.
[4] Molnár Z, Rockland KS. Chapter 5—cortical columns. In: Rubenstein J, Rakic P, Chen B, editors. Neural circuit and cognitive development (second edition). Academic Press; 2020. p. 103–26.
[5] Duraivel S, Rahimpour S, Chiang C-H, et al. High-resolution neural recordings improve the accuracy of speech decoding. Nat Commun 2023;14:6938.
[6] Viventi J, Kim D-H, Vigeland L, et al. Flexible, foldable, actively multiplexed, high-density electrode array for mapping brain activity *in vivo*. Nat Neurosci 2011;14:1599–605.
[7] Chiang C-H, Won SM, Orsborn AL, et al. Development of a neural interface for high-definition, long-term recording in rodents and nonhuman primates. Sci Transl Med 2020;12:eaay4682.
[8] Garcia-Cortadella R, Schwesig G, Jeschke C, et al. Graphene active sensor arrays for long-term and wireless mapping of wide frequency band epicortical brain activity. Nat Commun 2021;12:211.
[9] Wu M, Yao K, Huang N, et al. Ultrathin, soft, bioresorbable organic electrochemical transistors for transient spatiotemporal mapping of brain activity. Adv Sci 2023;10:2300504.
[10] Shaik FA, Ihida S, Ikeuchi Y, et al. TFT sensor array for real-time cellular characterization, stimulation, impedance measurement and optical imaging of *in-vitro* neural cells. Biosens Bioelectron 2020;169:112546.
[11] Londoño-Ramírez H, Huang X, Cools J, et al. Multiplexed surface electrode arrays based on metal oxide thin-film electronics for high-resolution cortical mapping. Adv Sci 2024;11:2308507.
[12] Huang X, Londoño-Ramírez H, Ballini M, et al. Actively multiplexed μecog brain implant system with incremental-δσ ADCS employing bulk DACS. IEEE J Solid State Circuits 2022;57:3312–23.
[13] Boran E, Ramantani G, Krayenbühl N, et al. High-density EEG improves the detection of high frequency oscillations that predict seizure outcome. Clin Neurophysiol 2019;130:1882–8.
[14] Kang W, Ju C, Joo J, et al. Closed-loop direct control of seizure focus in a rodent model of temporal lobe epilepsy via localized electric fields applied sequentially. Nat Commun 2022;13:7805.
[15] Devinsky O, Vezzani A, O'Brien TJ, et al. Epilepsy. Nat Rev Dis Primers 2018;4:18024.

Supplementary material

Device Fabrication

The device fabrication process was described as follows (Fig. S1 online): (1) A 200 nm thick Mo layer was sputtered onto a pre-cleaned PI substrate (25 μm thick) to form the bottom gate, followed by lithographic patterning; (2) Silicon nitride (SiN_x) and silicon dioxide (SiO_2) (200 nm / 200 nm) films were grown via plasma enhanced chemical vapor deposition (PECVD) as the gate insulating layers; (3) A 30 nm thick Ln-IZO semiconductor layer was sputtered as the TFT channel; (4) A 200 nm thick SiO_2 layer was deposited via PECVD as the source/drain insulating layer; (5) An etch barrier layer was dry-etched and patterned to protect the active layer, followed by sputtered Mo films (200 nm thick) to form the source/drain electrodes; (6) A 2 μm thick PI layer was spin-coated and patterned as the organic insulating layer; (7) A 200 nm thick Mo film was sputtered and patterned to form interconnects; (8) A 2 μm thick PI film was spin-coated and patterned as the insulation; (9) 5 nm Ti/100 nm Au films was evaporated onto the drain electrode to form sensing pads; (10) The sample was cut into individual arrays using a laser scriber; (11) Flexible device arrays are peeled off from the glass substrate.

Subsequently, the array was connected to a flexible printed circuit (FPC) via anisotropic conductive films (ACFs) through thermal pressing. The other end of the FPC was inserted into a zero-insertion force (ZIF) connector on a printed circuit board (PCB) to link with the data acquisition (DAQ) system.

Role of lanthanide doping in Ln:IZO

Lanthanide doping in IZO active layers has been reported to effectively suppress oxygen-vacancy–related defect states, thereby reducing threshold-voltage shifts and enhancing stability under negative bias illumination stress. This doping strategy also allows fine control

of carrier density without severely compromising mobility. By contrast, conventional dopants such as Sn, Ga, and Al mainly enhance conductivity and transparency but are less effective in mitigating oxygen-vacancy–induced instabilities. Consequently, Ln:IZO offers a favorable trade-off between mobility, bias stability, and low off-state leakage, which is essential for reliable device operation[1].

Data Acquisition System

The DAQ system was configured using PXIe-6739 and PXIe-4309 modules (National Instruments Corp.), with the PXIe-6739 as the input module and the PXIe-4309 as the output module. The DAQ system connects to the flexible array (attached on the PCB) via very high-density cable interconnect (VHDCI) cables. The input and output modules were managed via a LabVIEW software program (National Instruments Corp.) developed to support multiple channel configurations (e.g. 64 × 64 = 4096, 23 × 64 = 1472, etc.) and physical sampling rates (e.g. 250 S/s, 1000 S/s, etc.). During experiments, the PXIe-4309 was set to a maximum single-channel sampling rate of 100 kS/s with an oversampling ratio of 6.25 to achieve higher precision. For scanning, a control pathway from the PXIe-6739 output was connected to the G1 line signal to provide a marker for multiplexed signal alignment, ensuring accurate signal synchronization. The entire system utilized three PXIe-4309 cards and one PXIe-6739 card. Each PXIe-4309 card contains eight ADCs, with each ADC supporting four acquisition channels. Typically, three PXIe-4309 cards were used to record signals from 64 S lines. For the higher precision mode, each PXIe-4309 could be set to acquire from no more than eight S lines, enabling the use of only one channel per ADC.

in vitro Characterization

Morphological Characterization

Optical images at various magnifications were captured using an optical microscope (XZJ-L2030, Phenix). Cross-sectional images of devices were obtained using FIB-SEM (QUANTA 200 FEG, FEI).

Electrical Characteristics of individual TFTs

Transfer characteristics (I_{ds}–V_{gs}), output characteristics (I_{ds}–V_{ds}), and capacitance characteristics (C–V_{gs}) of individual TFTs were measured using a semiconductor device parameter analyzer (Keysight B1500A, Keysight Technologies). The frequency response curve was obtained by applying 1 mVpp sine waves with different frequencies to the drain electrode and measuring V_{out}/V_{in}. Additionally, the TFT array was immersed in a PBS solution, and linear voltage (from −10 mV to +10 mV) or sinusoidal signals (500 μVpp, 12 Hz) were applied using a platinum mesh electrode. *in vitro* impedance (vs. frequency) of the TFT was measured in PBS with an electrochemical workstation (CHI 650E, Shanghai Chenhua Co., Ltd, China).

Biocompatibility Characterization

For the cell viability test, a small TFT array (1.6 × 1.6 mm^2) was transferred on glass. Before cell culture, the sample was coated with 0.01% poly-l-lysine (No. P8920, Sigma-Aldrich) overnight, then coated with 1-2 μg cm^{-2} laminin (No. L2020, Sigma-Aldrich) for more than 4 hours. Dorsal root ganglia (DRG) of male rats (4 weeks) were excised and transferred in DMEM/F12 (No.11330-032, Gibco) on ice. Tissues were cut into small pieces and digested in an enzyme solution containing 5 mg ml^{-1} dispase (No.ST2339, Beyotime) and 1 mg ml^{-1} collagenase (No.ST2294, Beyotime) at 37 ℃ for 1 h. Then the samples were triturated with 1 ml pipette for 30 times until the liquid becoming turbid. After centrifugation

at 250 g for 5 min, cells were washed in 2 ml of DMEM/F12 + 15% (w/v) bovine serum albumin (No.SRE0096-10G, Sigma) and resuspended in 2 ml of DMEM/F12 + 10% fetal bovine serum (No.F802A, i-presci scientific) + 1% penicillin–streptomycin (No.15140-122, Gibco). 10% of the total DRG cells were seeded on the TFT device or standard glass coverslip in each well of the 96 wells plate. The DRG cells were cultured in an incubator at 37 ℃ for 1 day. For the assay, the samples were labeled with Calcein/PI Cell Viability/Cytotoxicity Assay Kit (Beyotime). Live cells were labeled with Calcein AM (green), and dead cells were labeled with Propidium Iodide (red). After adding the dyes, the samples were incubated for 30 min at 37 ℃ with 5% CO_2. The samples were washed with HBSS for three times. The viability (%) was calculated as total No. of live cells / total No. of cells $\times 100$.

Mechanical Testing

The flexible array was mounted on an in-situ mechanical testing platform (IBTC-300SL, Care Corp.) for bending tests, with a bending radius set to 5 mm and repeated 10,000 times. The array was then immersed in a PBS solution and driven by a platinum mesh electrode with a 2 mVpp, 12 Hz sine wave. Using the DAQ system, the array was scanned in time-division multiplexing mode with 4096 channels activated at an equivalent sampling rate of 250 S/s. The number of undamaged channels and the average gain were recorded.

Noise Characterization

The array was immersed in $1\times$ PBS solution (pH = 7.4, Sigma-Aldrich), with a platinum mesh electrode providing a ground signal. In the static mode, the DAQ system makes one G line active while keep other G lines closed, to record noise levels at different sampling rates. When recording from only 23 S lines one of the 24 available channels is reserved for capturing the switch calibration signal, and each of the remaining 23 ADCs was configured

with a single acquisition channel to achieve higher precision and lower noise. When recording from 64 S lines, all 24 ADCs were used, with each ADC handling 2 or 3 acquisition channels. In the dynamic mode, noise measurements were conducted under three different configurations: 64 (S) × 64 (G) = 4096 channels at 250 S/s, 24 (S) × 64 (G) = 1536 channels at 250 S/s, and 24 (S) × 16 (G) = 384 channels at 1000 S/s. In each configuration, the total sampling rate for each S line was fixed at 100 kS/s.

In-vitro mapping testing

A drop of 1× PBS solution (pH = 7.4, Sigma-Aldrich) was placed on the array, and a 1 mVpp, 18 Hz sine wave was input using a tungsten probe. The DAQ system recorded data from the 4096-channel array at a sampling rate of 250 S/s.

in vivo experiments

Animal Surgery

All animal procedures described in this study were approved by the Tsinghua University Institutional Animal Care and Use Committee (IACUC). Adult male New Zealand white rabbits (*Oryctolagus cuniculus*) (2000–2500 g) were purchased from Beijing Fangyuan Experimental Animal Technology Co., Ltd. and were housed individually under standard conditions. The animals were maintained on a 12-hour light/dark cycle at 22–25 ℃, with ad libitum access to food and water.

After weighing the rabbits, they were anesthetized using a combination of Xylazine (6.5 mg/kg) and Zoletil (13 mg/kg) administered intramuscularly. Additional doses, at one-quarter of the initial dose, were given every 30 minutes during the procedure. Anesthesia was verified by pinching the animal's hind limbs before starting the surgery. Meloxicam (0.3

mg/kg) was administered pre-operatively for pain relief, and erythromycin ointment or medical petroleum jelly was applied to protect the eyes. The anesthetized rabbit was secured in a stereotaxic frame and maintained on a warming pad to stabilize body temperature. The head was shaved, disinfected with 75% ethanol (Sigma-Aldrich), and the scalp was incised to expose the skull. The skull was aligned parallel to the reference plane of the positioning instrument, adjusted based on the rabbit's cranial sutures. The exposed skull was etched with 8% hydrogen peroxide (Sigma-Aldrich). A craniotome with a 1.2 mm diameter was used to create a hole in the target area of the skull, with continuous saline irrigation to prevent overheating of the brain. A 1.4 mm diameter stainless steel screw was inserted as a reference electrode. The dura mater was removed using curved surgical forceps and scissors, and a sterile, saline-soaked cotton ball was placed over the exposed brain to maintain moisture.

Epilepsy Induction and Acute ECoG Recording

The skull screw was grounded with a metal wire and connected to the DAQ system. A glass syringe needle was implanted near the hippocampus (AP: 4 mm, ML: 2.5 mm, DV: −2.3 mm). Penicillin G potassium (1000 IU in 2 μL/min, MCE) was injected into the hippocampus at a concentration of 200 IU/μL. After removing the needle, the NeuroCam array were placed on the cortex and held with hemostatic sponges in place.

Array Characterization and Data Processing

All data processing and analysis were conducted using Origin (OriginLab) and MATLAB (MathWorks). Recorded data were initially segmented in MATLAB. The timing of array row gating was determined based on the marker signal. The average of the more stable 3rd to 5th data points from 6 or 7 points in each row was used as the sampling value. This process was repeated for each column, converting the recorded 64 columns of data into a 64 × 64 array. The data were then filtered and smoothed in Origin: a 49–51 Hz band-stop

filter was used to remove power-line noise, followed by a 1–199 Hz band-pass filter to isolate the ECoG signals, and Savitzky-Golay smoothing was applied. Time-frequency plots, heatmaps, correlation analyses, and RMS analyses were performed using MATLAB functions such as ‘spectrogram’, ‘heatmap’, ‘corrcoef’, and ‘rms’. Gaussian fitting for histograms was done using Origin’s Gaussian fitting function. Signals were divided into Delta (1–4 Hz), Theta (4–8 Hz), Alpha (8–12 Hz), Beta (12–30 Hz), and Gamma (30–125 Hz) bands, with Gaussian fitting means calculated. Different waveforms during seizures were categorized into eight types using PCA and k-means clustering, with waveform and RMS heatmaps plotted. Three categories highly correlated with seizures were analyzed, producing delay heatmaps and spatial flow diagrams for the affected regions. Delay heatmaps were created by calculating the time differences between peak occurrences, illustrating the propagation of seizure waveforms. Spatial flow diagrams were generated by calculating the gradient of delay heatmaps, depicting the direction of seizure wave propagation.

References

[1] He P, Xu H, Lan L, et al. The effect of charge transfer transition on the photostability of lanthanide-doped indium oxide thin-film transistors. Communications Materials, 2021, 2: 86

Figure S1

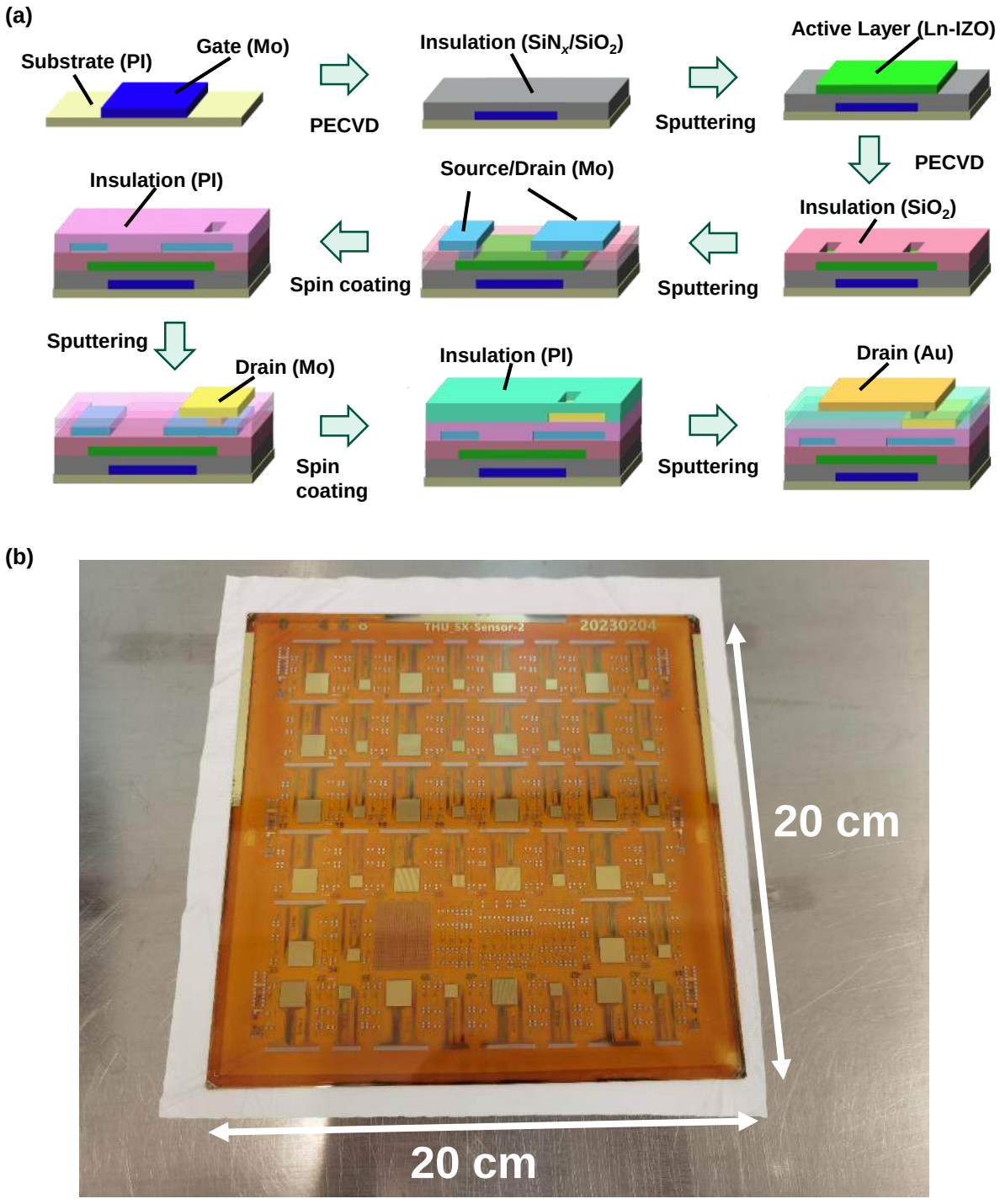

Figure S1. a. Process flow for device fabrication. **b.** Photograph of a fully-formed, large-area (20 cm × 20 cm) flexible sheet comprising multiple (>40) TFT arrays of different geometries laminated on glass.

Figure S2

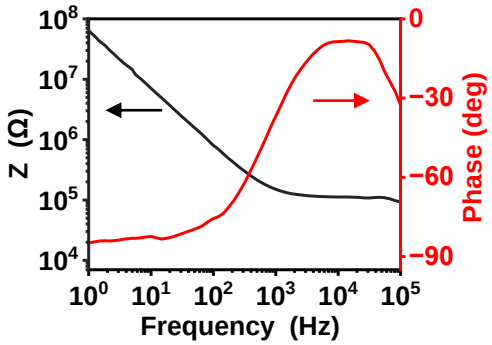

Figure S2. Impedance vs. frequency characteristic curve at V_{gs} = 6 V.

Figure S3

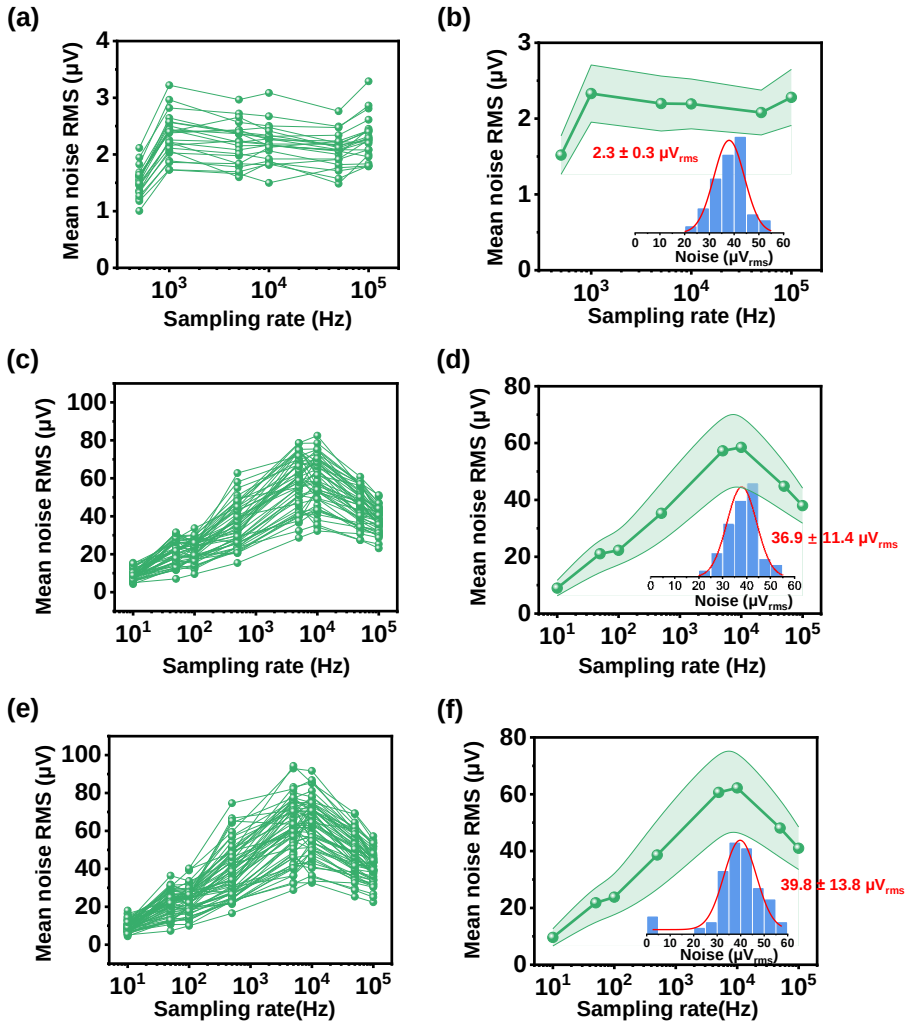

Figure S3. Noise characteristics of the NeuroCam system at the static mode. The array is immersed in PBS, and the input signal is applied using a platinum mesh electrode. One G line is kept on. **a.** Mean noise RMS result over 1 second from 23 S lines at various sampling rate. **b.** Statistical results of mean noise RMS for these 23 channels. Inset: Histogram and Gaussian fit curve of noise levels for all channels at a sample rate of 100 kS/s. **c.** Mean noise RMS result over 1 second from all 48 S lines at various sampling rate. **d.** Statistical results of mean noise RMS for these 48 channels. Inset: Histogram and Gaussian fit curve of noise levels for all channels at a sample rate of 100 kS/s. **e.** Mean noise RMS result over 1 second from all 64 S lines at various sampling rate. **f.** Statistical results of mean noise RMS for these 64 channels. Inset: Histogram and Gaussian fit curve of noise levels for all channels at a sample rate of 100 kS/s.

Figure S4

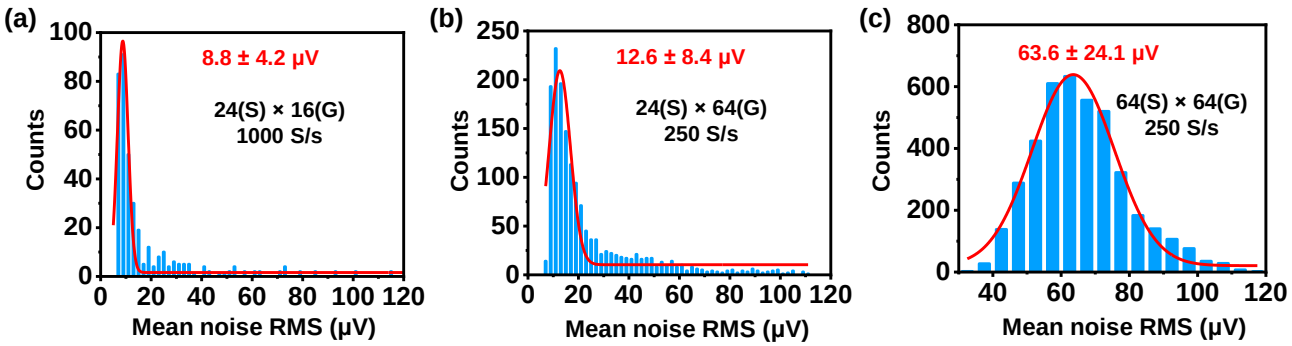

Figure S4. Noise characteristics of the NeuroCam system at the dynamic mode. The array is immersed in PBS, and the input signal is applied using a platinum mesh electrode. The sample rate for each S line is fixed at 100 kS/s. By adjusting the number of operated active lines (S and G), effective sample rates for each channel can be varied and corresponding noise levels are different. Effective sample rates for operating 24(S) × 16(G), 24(S) × 64(G), 64(S) × 64(G) are 1000 S/s, 250 S/s and 250 S/s, respectively.

Figure S5

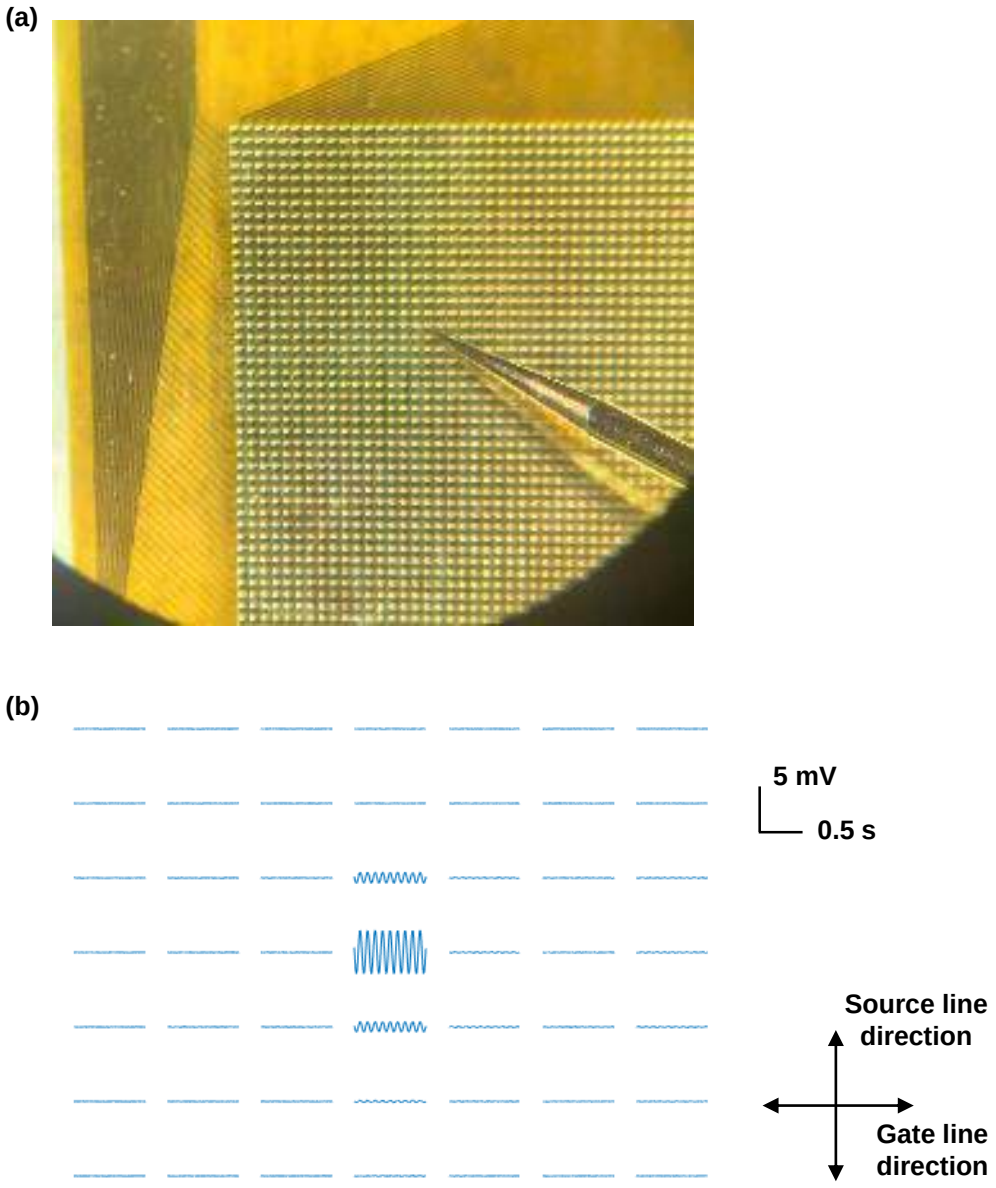

Figure S5. Crosstalk analysis of the NeuroCam array. a. Photograph showing a device array exposed in air, with a contact probe positioned on a single pixel and applying a sinusoidal signal (5 mVpp, 12 Hz). **b.** Measured output voltages from the probed pixel and its adjacent pixels. With only one point as the input signal, it can be observed that the other points are almost unaffected. Adjacent pixels in the direction of source line receives higher crosstalk signals (−12.6 dB) comparing to those in the direction of gate line (−37.2 dB), while second nearest neighboring and further pixels show minimal crosstalk signals (−45 dB).

Figure S6

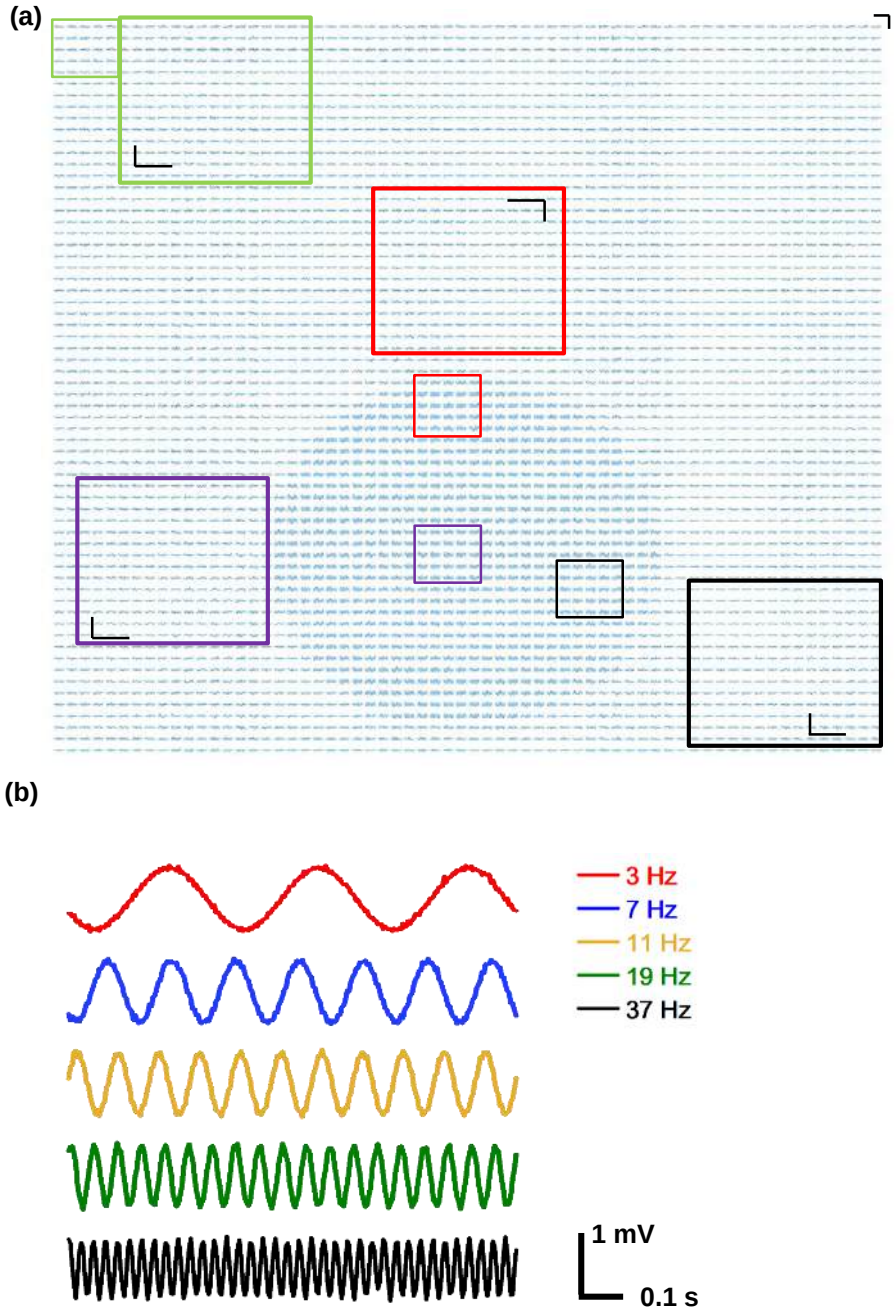

Figure S6. ***In vitro*** **recording signals from all 4096 channels in the TFT array. a.** A droplet of PBS is placed on the device surface, and a 1 mVpp sine signal (18 Hz) is applied into PBS. Insets show enlarged plots from different regions. Scalebars are 0.5 s and 1 mV. **b.** Signals recorded when injecting signals at different frequencies (3 Hz, 7 Hz, 11 Hz, 19 Hz, and 37 Hz) in PBS solution environment, corresponding to delta, theta, alpha, beta, and gamma bands of ECoG signals, respectively.

Figure S7

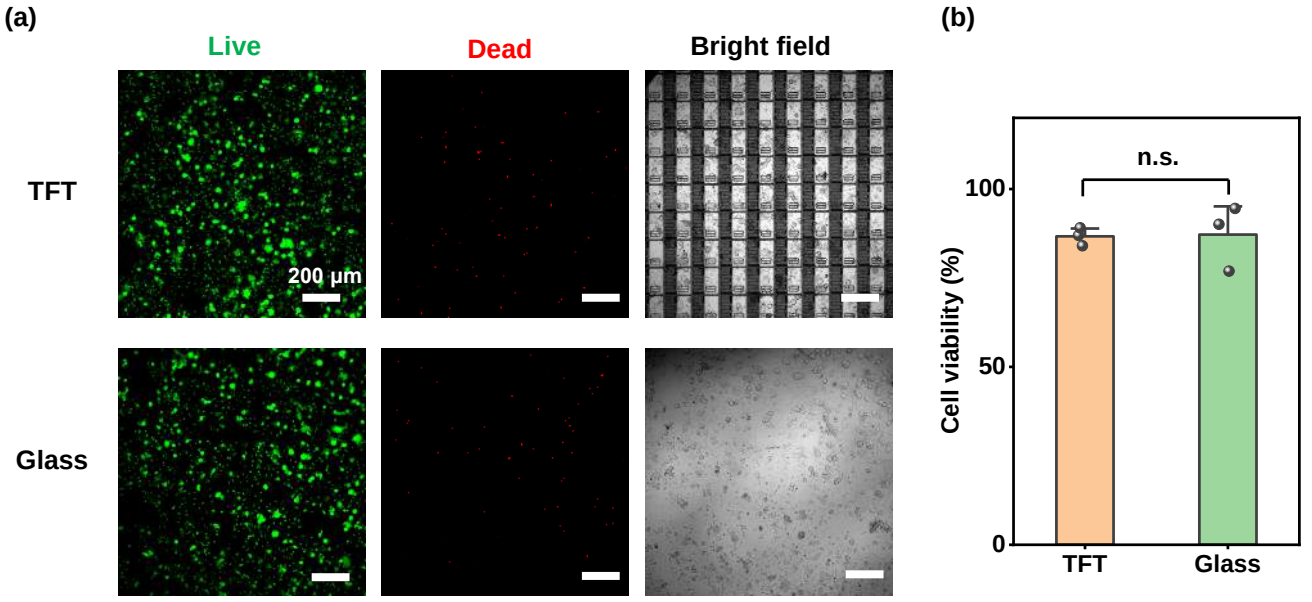

Figure S7. Biocompatibility of the TFT array. a. Live/dead fluorescence assay performed on DRG cells cultured on the TFT and glass for 24 h. Green (Calcien AM) and red (Propidium Iodide, PI) denote live cells and dead cells, respectively. **b.** Averaged viability (%) of DRG cells cultured on the TFT and glass. Data are presented as mean ± s.e.m. (*n* = 3 devices) and analyzed by unpaired *t*-test. n.s., not significant.

Figure S8

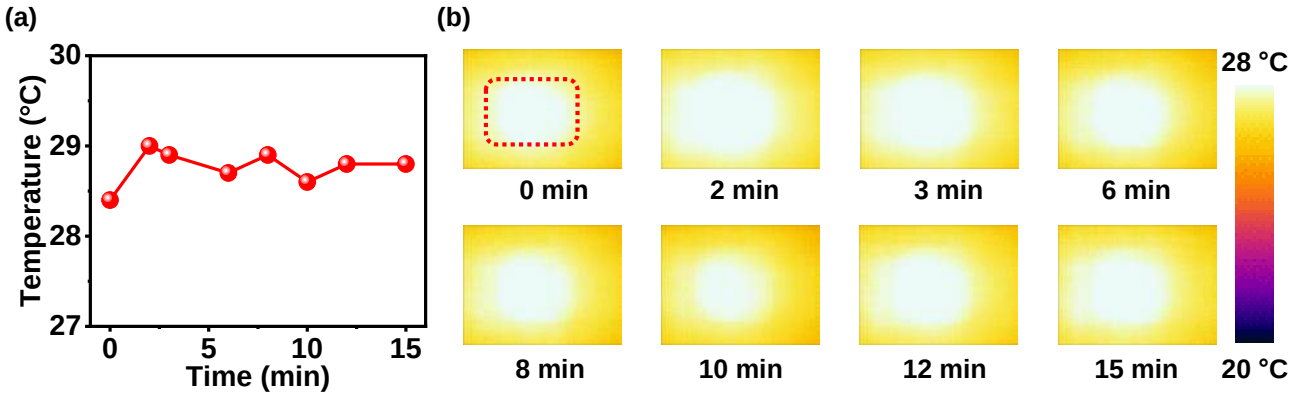

Figure S8. Thermal properties of the TFT array during operation. a. Plot of measured maximum surface temperature as a function of operation time. **b.** Thermography of a device array at different time points. During device operation, the maximum temperature is less than 29 ℃.

Figure S9

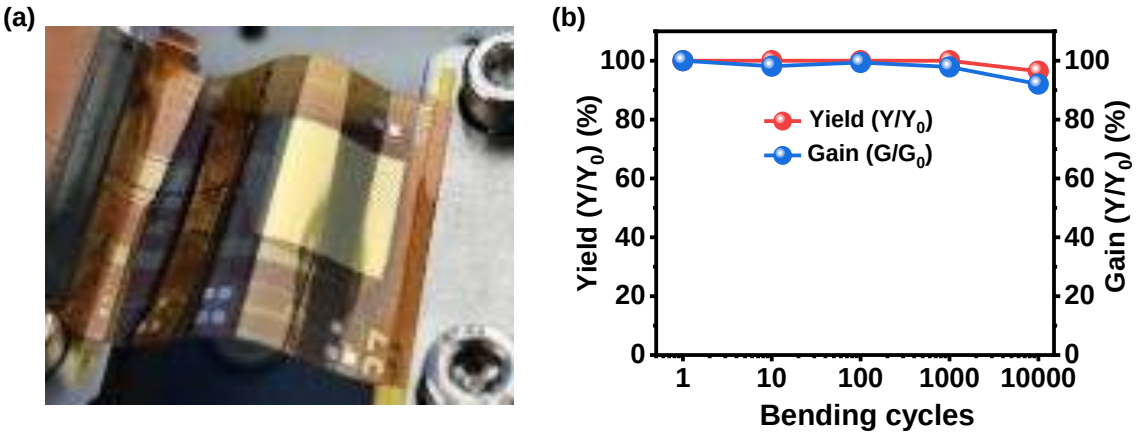

Figure S9. Mechanical properties of the TFT array. a. Experimental setup for dynamic bending test. **b.** Yield and average gain variation of the array under different bending cycles. The minimum bending radius is 5 mm. Yield is defined as the ratio of the number of channels functioning properly after bending to the number of channels functioning before bending. Gain is defined as the ratio of the average signal amplitude of all functioning channels after bending to the average signal amplitude before bending.

Figure S10

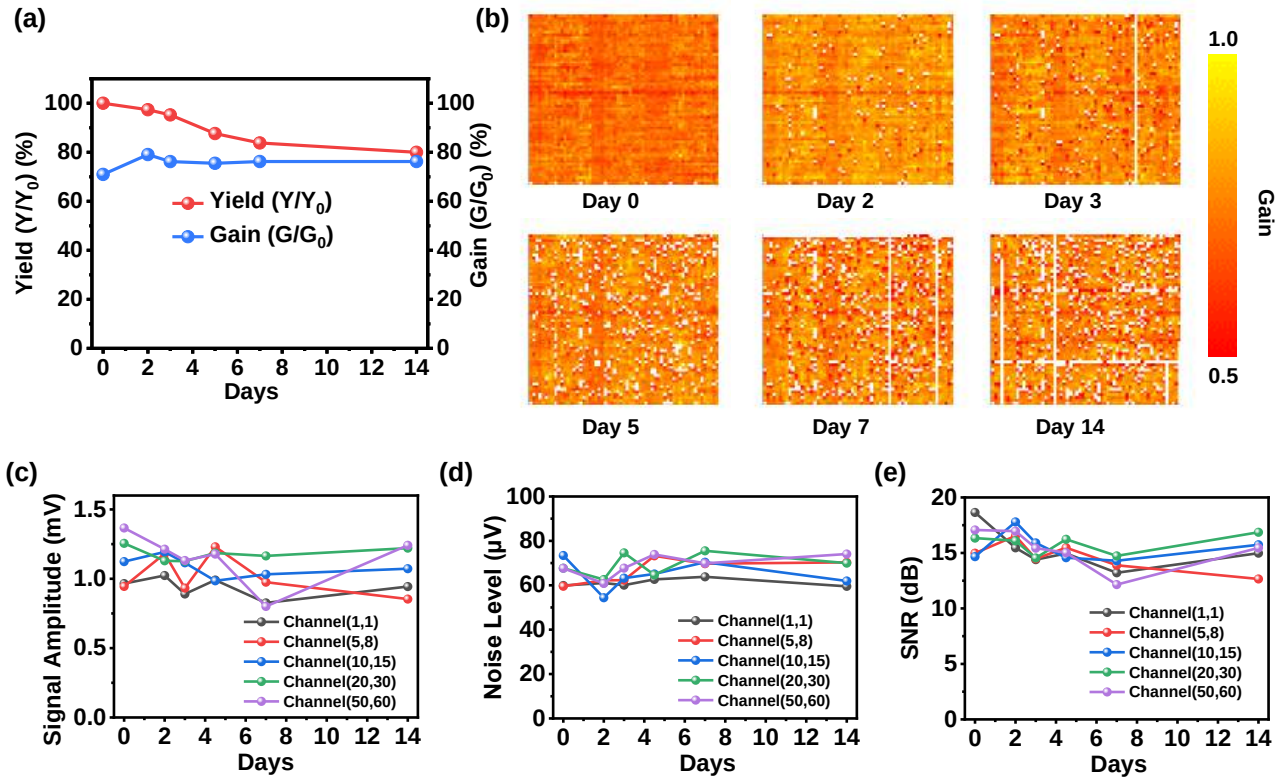

Figure S10. Performance of the TFT array during chronic soak test in PBS solution at 37 ℃. a. Variation of device yield and gain over soaking time. **b.** Measured spatial distribution of gain for all channels at different time points. **c–e.** Temporal evolution of the signal quality collected from five representative channels. **c.** signal amplitude. **d.** noise level. **e.** signal-to-noise ratio (SNR).

Figure S11

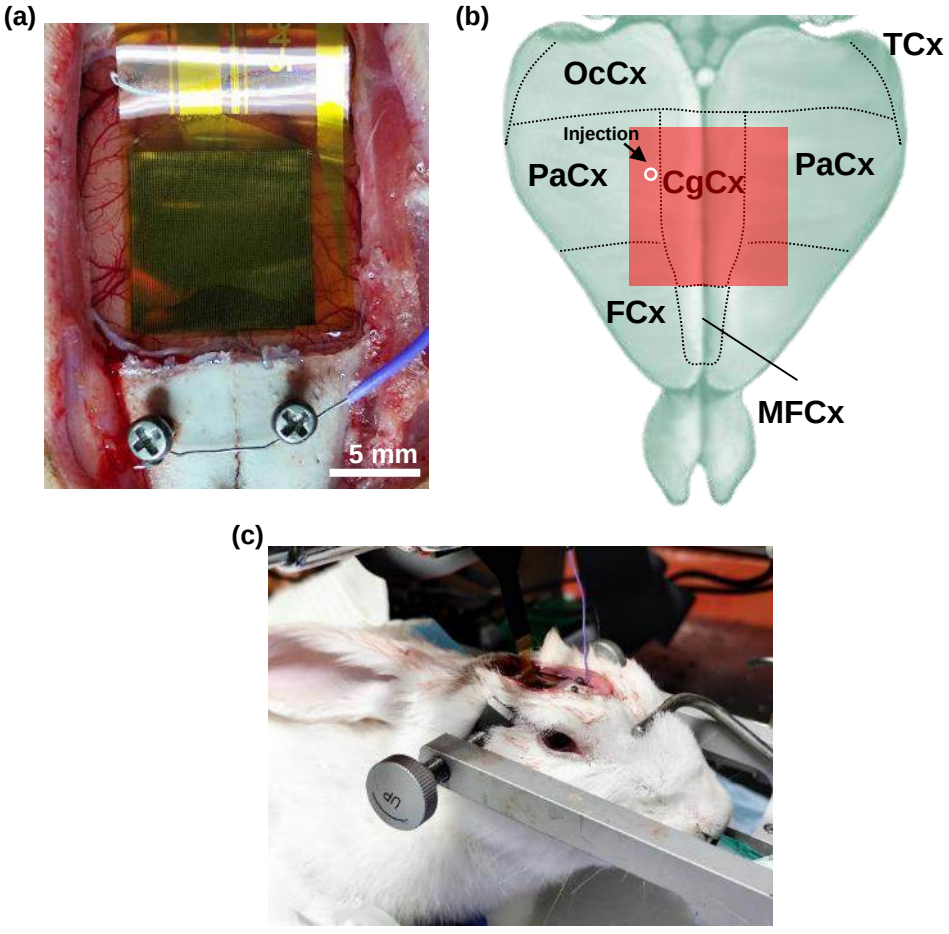

Figure S11. Setup for *in vivo* experiment using a rabbit model. a. A NeuroCam array placed on the cortex. **b.** Schematic illustration of the device array overlaid with segmented cortical areas of the rabbit brain (dorsal view), including temporal cortex (TCx), occipital cortex (OcCx), parietal cortex (PaCx), cingulate cortex (CgCx), frontal cortex (FCx), medial frontal cortex (MFCx). The arrow indicates the location of penicillin injection. **c.** Wired device array used in an anesthetized rabbit.

Reference: E. Munoz-Moreno *et al.*, A Magnetic Resonance Image Based Atlas of the Rabbit Brain for Automatic Parcellation. *PLoS ONE* **8**, e67418 (2013).

Figure S12

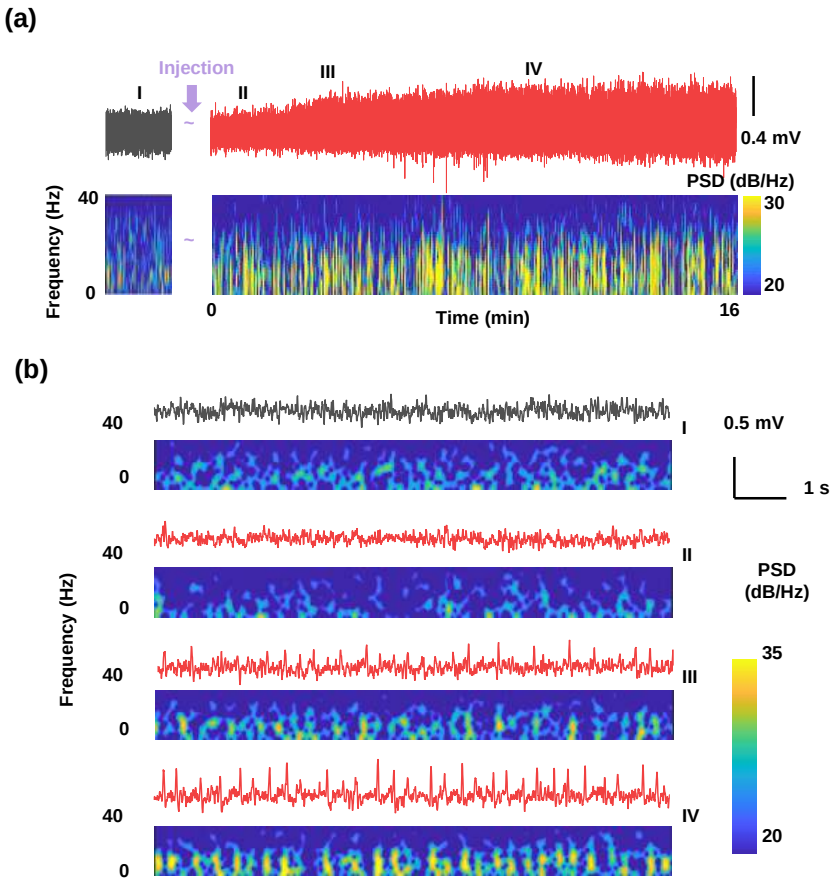

Figure S12. ***In vivo*** **recording of epileptiform activity in rabbits using the NeuroCam array.** **a.** Typical ECoG signals and their time-frequency patterns registered by a representative channel near the injection site before and during epileptic seizures. **b.** Temporally resolved ECoG signals in c. and corresponding time-frequency patterns at four different time points: (I) before penicillin injection, (II) shortly after injection, (III) onset of epilepsy, and (IV) status epilepticus.

Figure S13

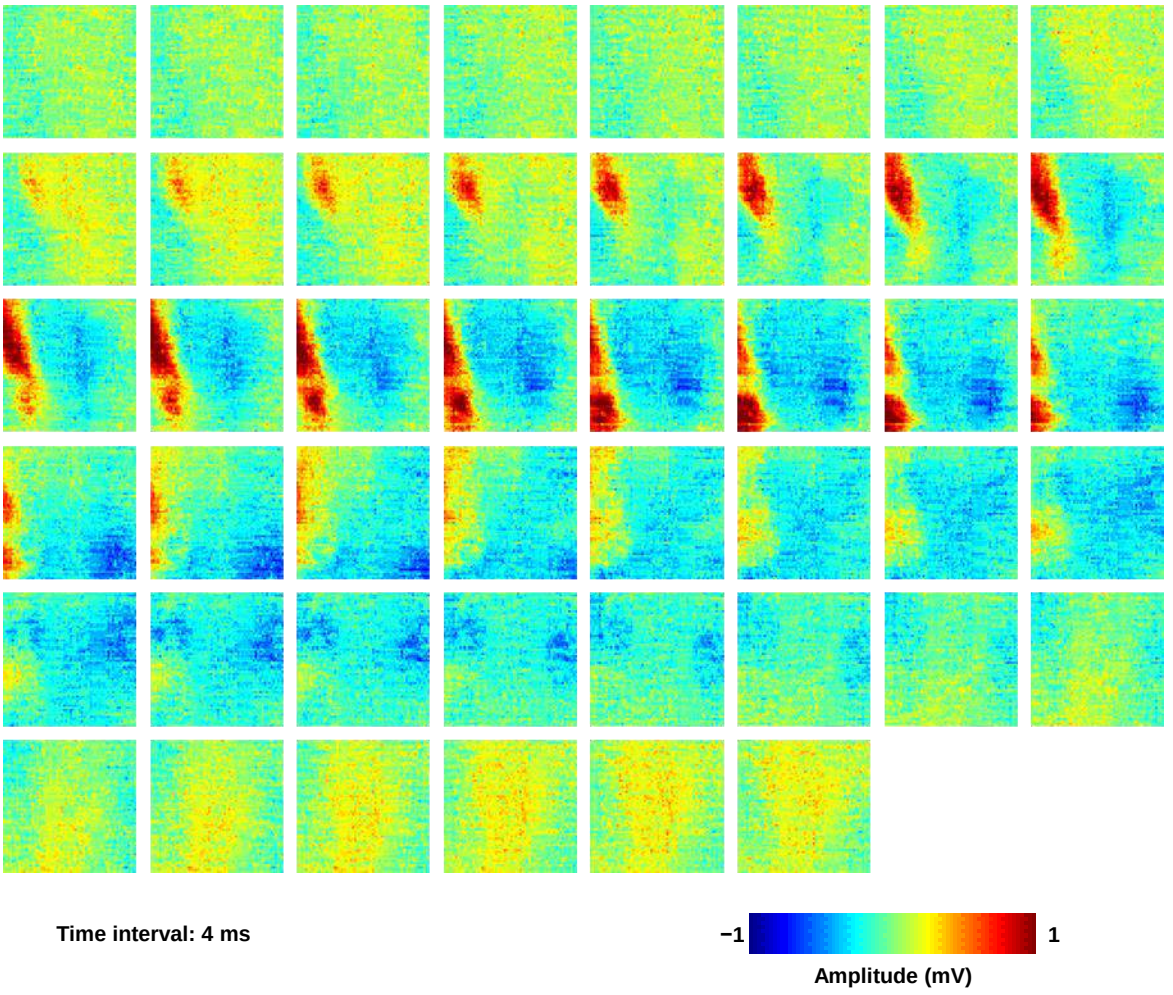

Figure S13. Time-lapse mapping results of a representative epileptic spike within 180 ms.

Figure S14

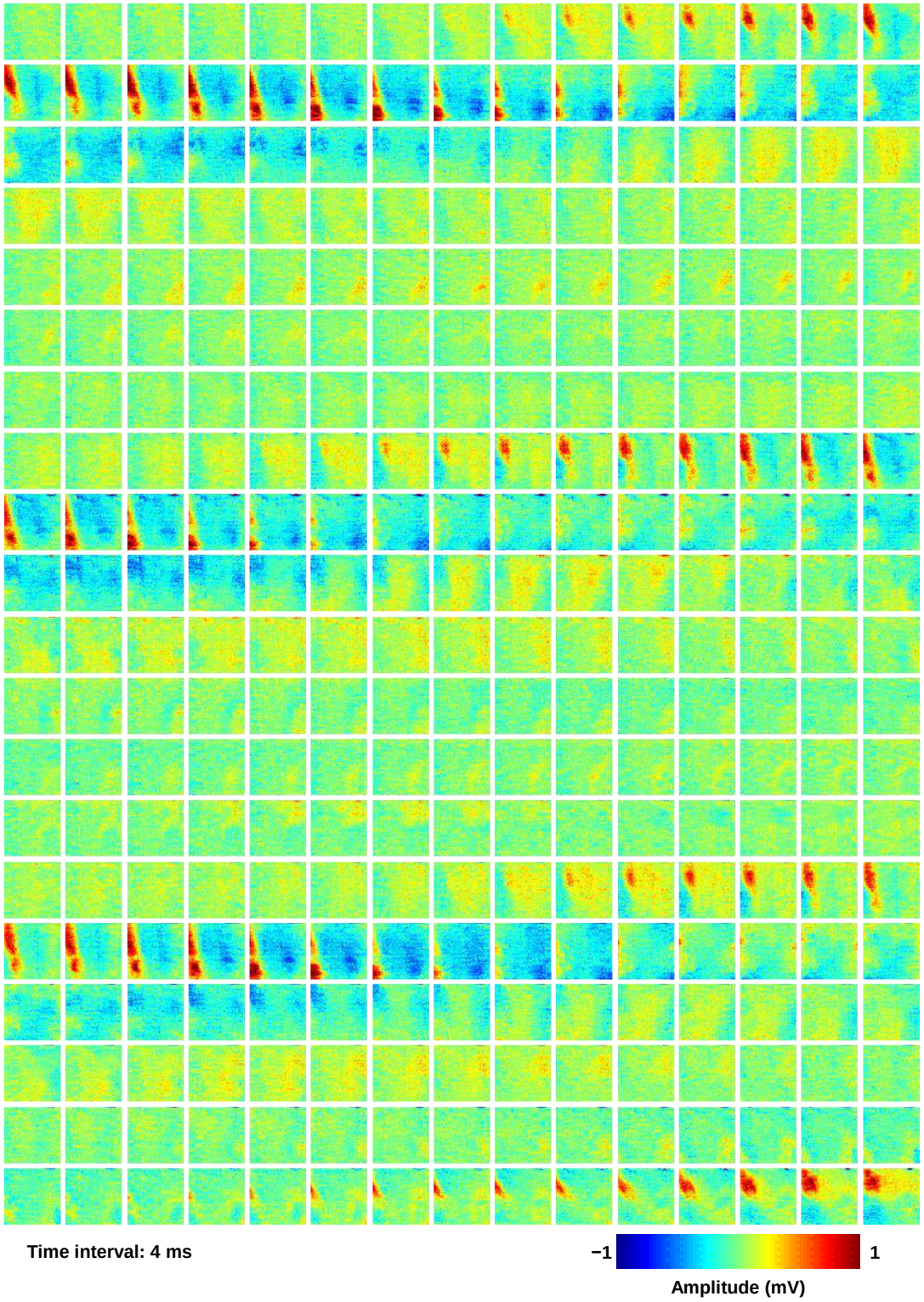

Figure S14. Time-lapse mapping results of three continuous epileptic spike waves within 1.2 s.

Figure S15

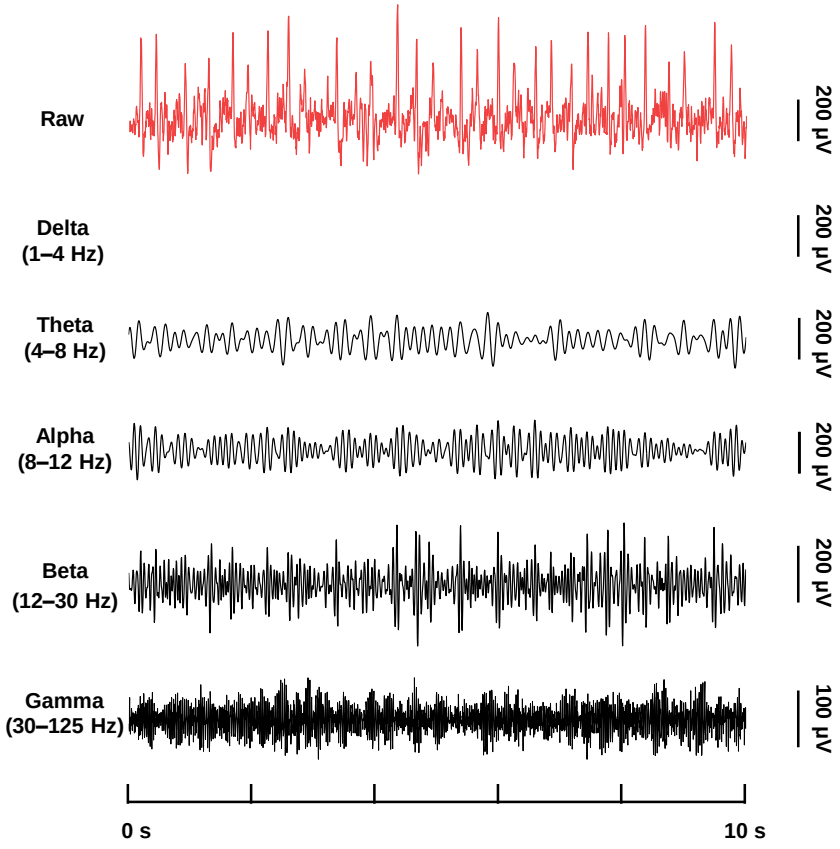

Figure S15. Raw ECoG data registered by a representative channel during epileptic seizures, and corresponding results in different frequency bands: Delta (1–4 Hz), Theta (4–8 Hz), Alpha (8–12 Hz), Beta (12–30 Hz), and Gamma (30–125 Hz).

Figure S16

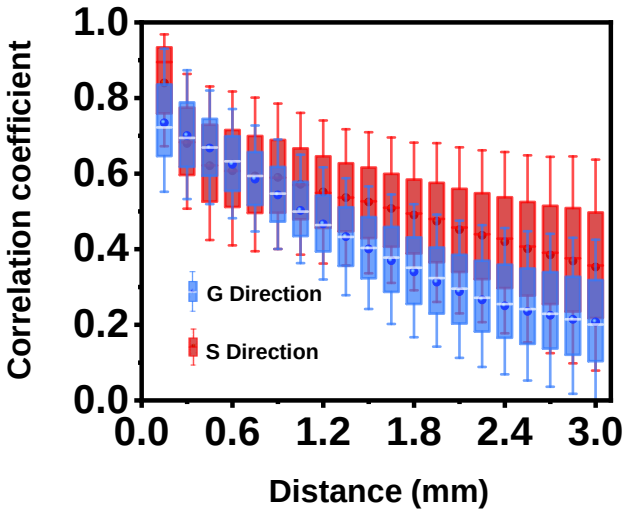

Figure S16. Relationship between correlation coefficients and inter-electrode distances, in the G and S directions.

Table S1

Work	TFT technologies	Channel no.	Density (sites / mm^2)	Pad size (μm^2)	Fan-in × fan-out
J. Viventi et al	Silicon	360	4	300 × 300	20 × 18
M. A. Escabí et al.	Silicon	196	12.25	200 × 200	14 × 14
R. Garcia-Cortadella et al	Graphene	32	4.35	50 × 50	4 × 8
N. Schaefer et al.	Graphene	64	6.25	50 × 50	8 × 8
C.-H. Chiang et al.	Silicon	1008	12.12	100 × 180	28 × 36
R. Garcia-Cortadella et al.	Graphene	64	6.25	50 × 50	6 × 11
M. Wu et al.	PEDOT:PSS	100	1.56	200 × 20	10 × 10
H. Londoño-Ramírez et al.	IGZO	256	4	Φ300	16 × 16
This Work	**Ln-IZO**	**4096**	**44.44**	**70 × 135**	**64 × 64**

Table S1. Comparison of characteristic parameters between this work and other multiplexed TFT-based μECoG arrays performed *in vivo* validation.

References:

1. Viventi, J. *et al.* Flexible, foldable, actively multiplexed, high-density electrode array for mapping brain activity *in vivo*. *Nat. Neurosci.* **14**, 1599-1605 (2011).
2. Escab ́ı M. A. *et al.* A high-density, high-channel count, multiplexed μECoG array for auditory-cortex recordings. *J. Neurophysiol.* **112**, 1566-1583 (2014).
3. Garcia-Cortadella, R. *et al.* Switchless Multiplexing of Graphene Active Sensor Arrays for Brain Mapping. *Nano Lett.* **20**, 3528-3537, (2020).
4. Schaefer, N. *et al.* Multiplexed neural sensor array of graphene solution-gated field-effect transistors. *2D Mater.* **7**, 025046 (2020).
5. Chiang, C.-H. *et al.* Development of a neural interface for high-definition, long-term recording in rodents and nonhuman primates. *Sci. Transl. Med.* **12**, eaay4682 (2020).
6. Garcia-Cortadella, R. *et al.* Graphene active sensor arrays for long-term and wireless mapping of wide frequency band epicortical brain activity. *Nat. Commun.* **12**, 211 (2021).
7. Wu, M. *et al.* Ultrathin, Soft, Bioresorbable Organic Electrochemical Transistors for Transient Spatiotemporal Mapping of Brain Activity. *Adv. Sci.* **10**, 2300504 (2023).
8. Londo ño-Ram írez, H. *et al.* Multiplexed Surface Electrode Arrays Based on Metal Oxide Thin-Film Electronics for High-Resolution Cortical Mapping. *Adv. Sci.* **10**, 2308507 (2023).

Movie S1

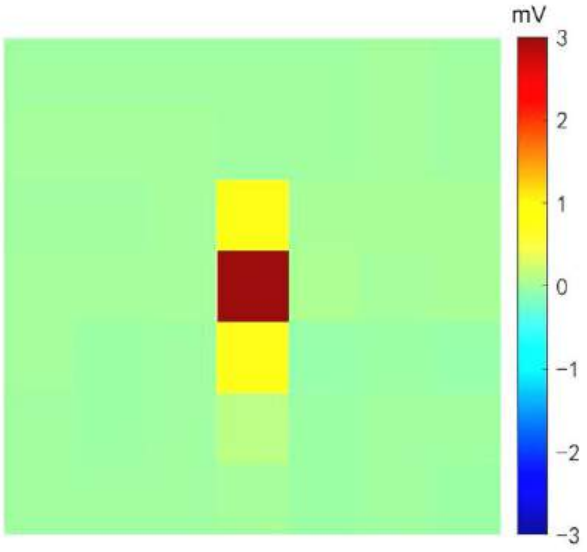

Movie S1. Slow motion video (0.1× speed) shows the crosstalk recorded by the NeuroCam array.

Movie S2

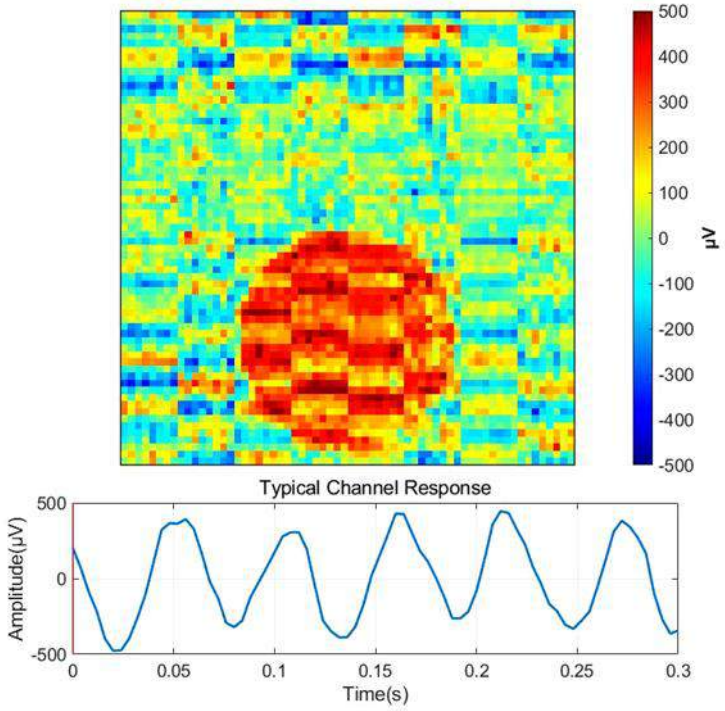

Movie S2. Slow motion video (0.1× speed) shows *in vitro* mapping results of spatially resolved output signals when injecting a 1 mVpp sine signal (12 Hz) into a PBS droplet with a circular shape on the NeuroCam array.

Movie S3

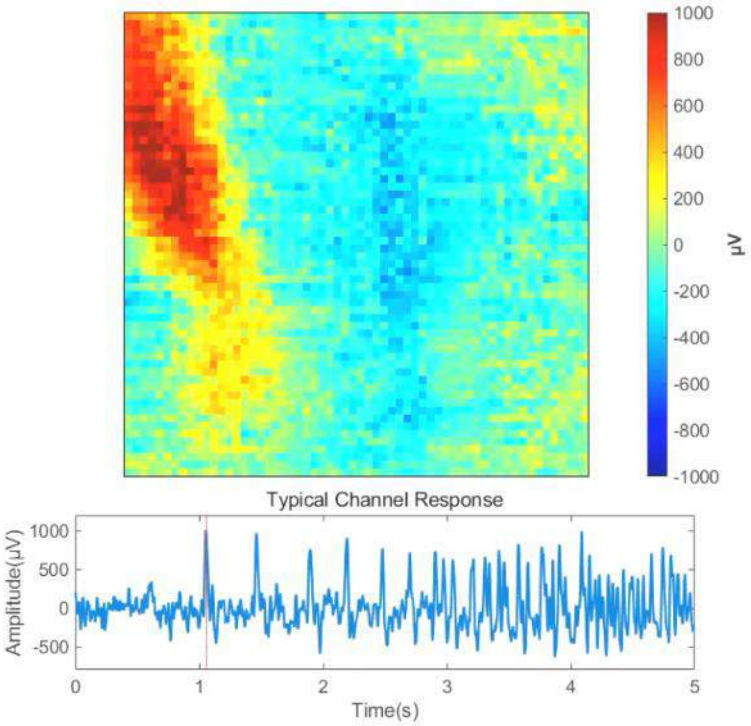

Movie S3. Slow motion video (0.1× speed) shows *in vivo* spatiotemporal evolution of epileptiform discharges captured by the NeuroCam array.